CELL BIOLOGY

Cell activity modulation and its specific function maintenance by bioinspired electromechanical nanogenerator

Tong Li[1†], Chuanmei Shi[1†], Fei Jin[1†], Fan Yang[2†], Long Gu[3], Ting Wang[4], Wei Dong[1], Zhang-Qi Feng[1]*

The biophysical characteristics of the extracellular matrix (ECM), such as a three-dimensional (3D) network and bioelectricity, have a profound influence on cell development, migration, function expression, etc. Here, inspired by these biophysical cues of ECM, we develop an electromechanical coupling bio-nanogenerator (bio-NG) composed of highly discrete piezoelectric fibers. It can generate surface piezopotential up to millivolts by cell inherent force and thus provide in situ electrical stimulation for the living cells. Besides, the unique 3D space in the bio-NGs provides an ECM-like growth microenvironment for cells. As a result, our bio-NGs effectively promote cell viability and development and, more importantly, maintain its specific functional expression. These advanced in vitro bio-NGs are expected to fill the gap between the inaccurate 2D systems and the expensive and time-consuming animal models, mimicking the complexity of the ECM and the physiological relevance of an in vivo biological system.

INTRODUCTION

Bioelectricity as a kind of biophysical cue is crucial guidance for cell proliferation/differentiation, embryonic development, and tissue regeneration. This endogenous bioelectricity exists in both the cytoplasm and extracellular space. With this foundation, electrical stimulation of excitable cells that can modulate the cell activity has therefore attracted great attention and offers broad application prospects for biomedical therapeutics (*1*–*4*). Most of these treatments require external energy input and wire connection, applying external electrical pulses to an undetermined group of cells through implanted microelectrodes (*5*, *6*). Long leads from the stimulator housing to the stimulation site will increase the risk after implantation including infection, loss in efficacy, and device failure, as well as electromagnetic interference, cross-talk, and power inefficiencies. Recent forwards in nanotechnology and smart materials allow electrodeless and battery-free treatments with autogenous excitation and high spatial resolution. Among them, electromechanical coupling nanogenerators (NGs) have been already used for biological applications such as brain stimulation, hair regeneration, wound healing, etc. (*4*, *7*–*11*), but they are still not a well-accepted solution for electrical stimulation of functional cells. A stimulating electrode element or in situ electrical stimulation unit is two-dimensional (2D) and usually causes functional cells (e.g., mesenchymal cells, muscle cells, neuronal cells, etc.) to lose their original morphology and specific functional expression (*12*, *13*).

Recognizing this defect, we seek solutions and turn to nature for inspiration. In biology, the extracellular matrix (ECM) is a 3D network of extracellular macromolecules, such as collagens, enzymes, and glycoproteins, that provide structural and biochemical support to surrounding cells (*14*). Among them, collagens are widely present in the ECM as fibrillar proteins and give structural support (i.e., 3D cell growth space) to resident cells. This collagen is also a kind of natural electromechanical conversion material, acting as a medium of bioelectric signal transmission and communication between cells (Fig. 1A) (*15*, *16*). Here, inspired by the biological function and microstructure of the collagen fibers in ECM, we presented an electromechanical coupling bio-NG composed of highly discrete piezoelectric electrospun fibers that provide cells with the "closer–to–in vivo" behavior. It could yield, in response to the inherent force produced by a single cell, a local electric field that stimulated and modulated their cell activity, without applying any additional external stimulation (Fig. 1B). In addition, our developed bio-NGs provided an ECM-like 3D growth microenvironment for cells. When cells were cultured in bio-NGs, the NG-cell interactions in 3D space triggered the opening of ion channels present in the plasma membrane of retinal ganglion cell 5 (RGC5), inducing intracellular calcium transients, and stimulated the motility of primary hepatocytes to form broad cell aggregates, as well as accelerated the differentiation of human mesenchymal stem cells (hMSCs) into osteoblasts. Besides, it was verified that the 3D space coupled with NG-cell interaction can coordinate to promote cell viability and development and, more importantly, maintain its specific functional expression. This bio-NG–cell interaction was also applicable in vivo, which could reduce inflammation, induce hepatocyte proliferation, and accelerate angiogenesis inside the regenerated tissues, thereby ultimately promoting liver repair. The electrode-less and battery-free methods for in situ electrical stimulation of cells in 3D space provided unlimited possibilities for future bioelectronic therapies, where controlled electrical impulses can replace the use of chemical drugs for disease treatment, nerve/tissue repair, and regeneration. More broadly, this work presented a practical strategy to fill the gap between bioelectricity in 3D space as a key biological phenomenon and wireless electrical stimulation of cells and tissues to repair or sustain cell function.

RESULTS

Formation of bioinspired electromechanical bio-NGs

Recently, some papers reported the piezoelectric properties of polyacrylonitrile (PAN) (*17*, *18*). Although it was generally established that PAN typically had low ferroelectricity, in comparison with polyvinylidene fluoride (the state-of-the-art piezoelectric polymer), PAN

[1]School of Chemistry and Chemical Engineering, Nanjing University of Science and Technology, Nanjing 210094, P. R. China. [2]Institute of Rail Transit, Tongji University, Shanghai 201804, P. R. China. [3]School of Advanced Materials and Nanotechnology, Xidian University, Xi'an 710071, P. R. China. [4]State Key Laboratory of Bioelectronics, Southeast University, Nanjing 210096, P. R. China.
*Corresponding author. Email: fengzhangqi1981@163.com
†These authors contributed equally to this work.

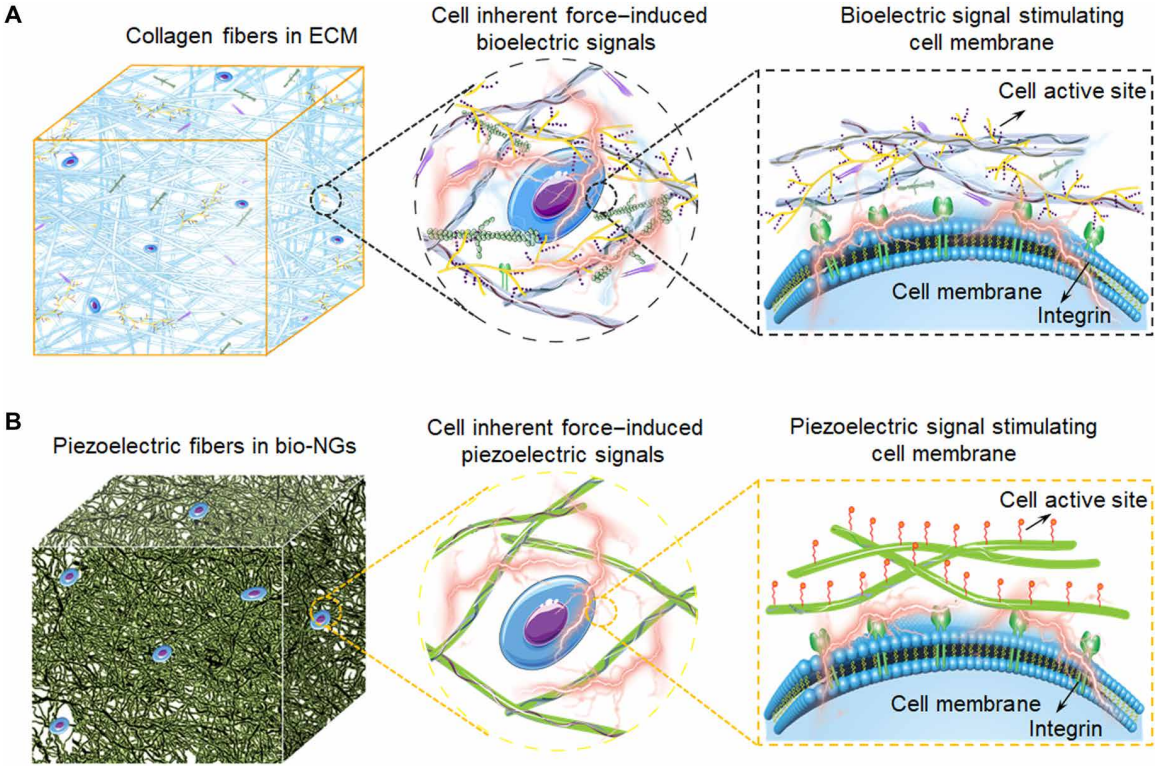

Fig. 1. Schematic illustrations of electromechanical coupling bio-NGs modulating cell activity inspired by ECM. (**A**) The collagen fibers in ECM converting the cell inherent force into bioelectricity, which also constitutes the 3D architecture of ECM. These bioelectric signals are transmitted by signal molecules filled between collagen fibers, thus, to regulate cell activity and realize the functional expression of cells. (**B**) Schematic diagram of the bioinspired piezoelectric fibers in bio-NGs. The interaction of cells with bio-NGs emulating this bioelectric signal in ECM induces, in response to the inherent forces produced by the cells, a local electric field that stimulates and modulates their cell activity.

had smaller dielectric loss and higher thermal stability and processability. In particular, the —CN groups on PAN can be hydrolyzed into —NH_2 groups and —COOH groups that facilitated cell adhesion and surface functionalization. This tight cell adhesion was essential for inducing the piezoelectric effect. Therefore, PAN was extremely suitable for the in situ cell-scale electrical stimulation. However, the narrow micropores among the close-packed fibers generally <2 μm of most current electrospun scaffolds were smaller than the cell size (average size, >5 μm). In this case, these scaffolds still combined with cells in nearly 2D growth mode and failed to provide the true 3D cell growth space. To address this issue, Fe_3O_4 magnetic nanoparticles were introduced into PAN electrospun solution to fabricate highly discrete Fe_3O_4/PAN fibers using a magnetic-assisted electrospinning device (Fig. 2A and fig. S1). In this electrospinning, the neodymium iron boron magnet could attract Fe_3O_4 nanoparticles doped in PAN fibers to break through water surface tension and, thus, to achieve 3D Fe_3O_4/PAN scaffolds with well-interconnected pores and discrete fibers for cell free migration.

In addition to the 3D space, the closer–to–in vivo living environment of cells also required another biophysical cue, bioelectricity. To improve this biophysical cue, poly(3,4-ethylenedioxythiophene) (PEDOT) exhibiting a high electronic conductivity and facile charge transfer and graphene oxide (GO) with excellent cell affinity were successively introduced onto the Fe_3O_4/PAN fibers via self-assembly processes. The introduction of the PEDOT layer was carried out to accelerate the interface charge transfer. The polymerization of EDOT on the surface of the Fe_3O_4/PAN fibers occurred in the reaction system of EDOT-$FeCl_3$ in anhydrous diethyl ether; a uniform PEDOT layer (~2 nm) formed under ultrasound in an ice water bath (Fig. 2B and fig. S2). Notably, the surface of the polymerized PEDOT in such reaction system was usually positively charged. Since GO was rich in anionic groups such as carboxyl and hydroxyl groups, it could be electrostatically adsorbed with PEDOT layer and, thereby, self-assemble into GO outer layer (~30 nm; Fig. 2B, fig. S3, and note S1), resulting in the target scaffold composed of uniform, randomly oriented fibers with diameters ranging from 400 to 900 nm (Fig. 2E, inset). This size range was between collagen fibrils and their bundles (10 nm to 10 μm; table S1). In this target scaffold, PEDOT was conducive to the transmission of bioelectric and piezoelectric signals, and the outermost GO layer acted as active sites for cell adhesion. The carbon skeleton in GO could be π-π conjugated with protein, and its polar groups could also attract hydrophilic functional groups of cells. These two synergistic effects promoted the exchange of information between cells. As a result, a series of well-interconnected micropores (89.38% porosity) with an average pore size of 18 ± 2 μm existed in this scaffold (Fig. 2, C to E, and fig. S4, A to C), thus ensuring that cells could migrate smoothly into the scaffold to form a cell 3D culture microenvironment (table S2) (*19*). Besides these macropores, many micro/mesopores <100 nm existed in this target scaffold (fig. S4D), which could further promote cell interaction/adhesion with fibers (*20*). Last, the electromechanical coupling bio-NGs assembled by this scaffold could yield local surface piezoelectric

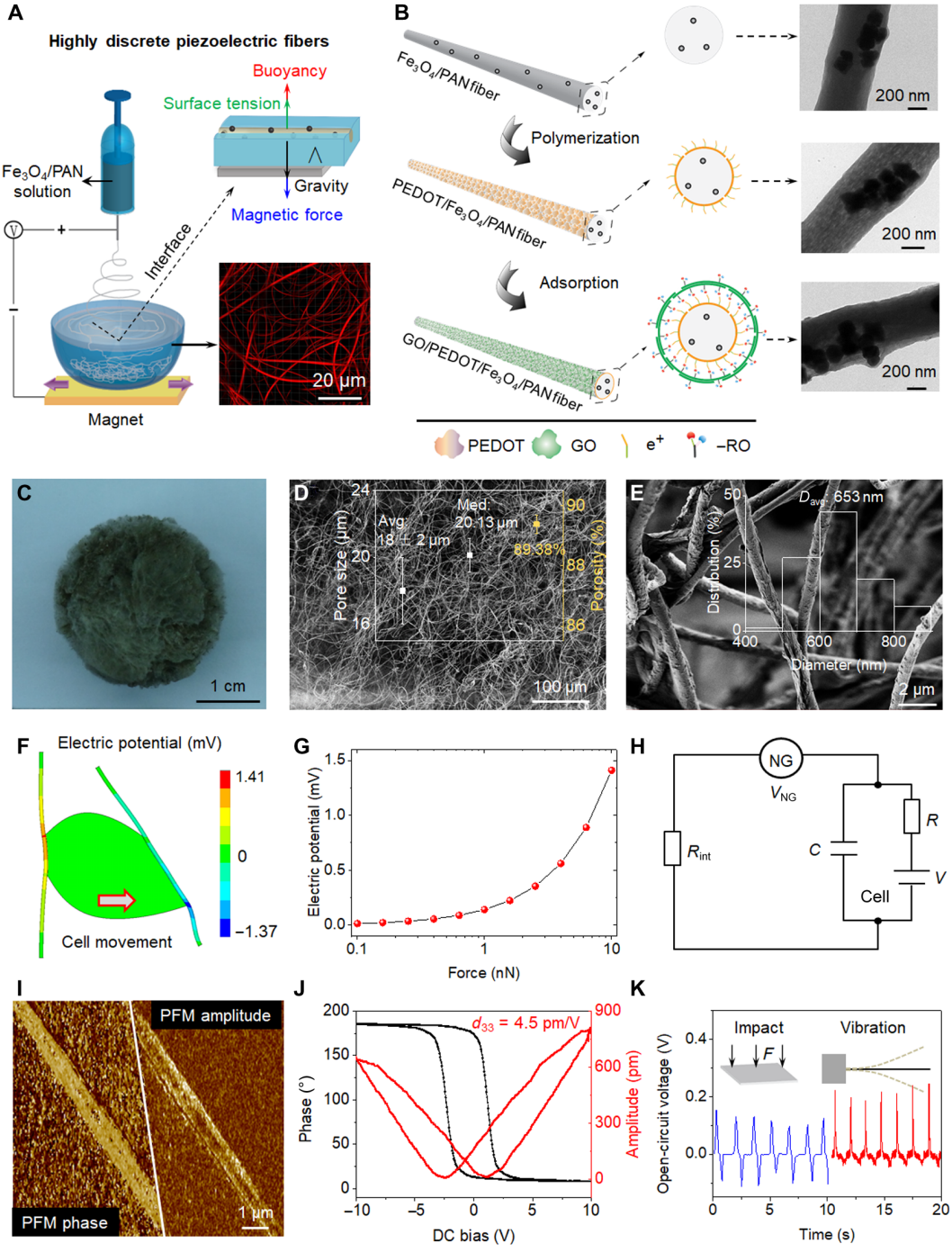

Fig. 2. Schematic representation and piezoelectric analysis of bio-NGs. (**A**) Schematic diagram of the fabrication of highly discrete piezoelectric Fe_3O_4/PAN fibers. With the help of the neodymium iron boron magnet, Fe_3O_4 magnetic nanoparticles were introduced into PAN electrospun solution to break through the surface tension of water. (**B**) The PEDOT conductive layer was loaded with the method of in situ polymerization; GO nanosheets were adsorbed on the outermost layer of fibers by the contribution of electrostatic adsorption force to form the target GO/PEDOT/Fe_3O_4/PAN fibers. Transmission electron microscopy images of the single fiber obtained in every step. (**C** to **E**) Optical image and scanning electron microscopy (SEM) images of the bio-NGs. The inset of (D) shows pore size distribution and porosity. The inset of (E) shows the fiber diameter distribution range of the GO/PEDOT/Fe_3O_4/PAN fibers. (**F**) Finite element analysis simulation of piezoelectric fibers coupled with a living cell generating a maximum voltage of 141 mV when strained by a tangential force of 10 nN. (**G**) Piezoelectric potential generated by a single fiber as a function of the applied tangential cell force. (**H**) Simplified resistor-capacitor circuit created by the NG, the NG-cell interface, and the cell membrane. (**I**) Piezoelectric force microscopy (PFM) phase and PFM amplitude images of a single fiber in bio-NGs. (**J**) Phase-electric potential hysteresis and butterfly amplitude loops of fibers in bio-NGs, obtained with a DC voltage varying from −10 to 10 V. (**K**) Voltage outputs from the bio-NGs under the same impact force of 1 N (blue) and under a vibration at 0.7 Hz (red). The inset represented the impact (left) and vibration (right) methods used to characterize the fibers in bio-NGs. F, force. Photo credit: Chuanmei Shi, Nanjing University of Science and Technology.

potential by the cell inherent forces, which would promote the transmission and communication of signals between cells, thus mimicking the bioelectric effects of collagen fibrils/fibers in ECM.

The piezoelectric potential generated from cell force in bio-NGs was simulated and studied by finite element analysis. Typically, mechanical stresses developed by cells were in the nanonewton range (0.1 to 10 nN). Two ends of the piezoelectric fibers were defined as anchors or fixed constraints, and a load force of 0.1 to 10 nN was applied at the cell-fiber contact. These stresses were sufficient to bend piezoelectric fibers and drive bio-NGs (Fig. 2F, fig. S5, and note S2). As a result, fibers in the bio-NGs yielded piezoelectric potential going from 14.1 μV to 1.41 mV with cell traction forces increased from 0.1 to 10 nN (Fig. 2G). This piezopotential was the theoretical open-circuit voltage along the fibers; however, the final voltage reaching the cell membrane would be affected by the conductivity of the NG-cell interface ($1/R_{int}$) and the electrical model of the cell membrane (Fig. 2H and note S3). Parallel to the theoretical piezoelectric potential, the piezoelectricity of a single fiber in bio-NGs was directly characterized by piezoelectric force microscopy (PFM; Fig. 2I). Strong and high phase contrast could be observed from the single fiber, matching well to the high contrast in the piezoelectric amplitude image. This suggested that the single fiber in bio-NGs has a large-area single piezoelectric domain along the fiber, which was greatly preferred for yielding high piezoelectric response under the cell traction forces. Its ferroelectricity was evidenced by the local electric field–polarization hysteresis obtained from the PFM phase and amplitude loops. As shown in Fig. 2J, our target fibers exhibited a clear hysteresis of 180° phase change and a butterfly-shaped hysteresis of the amplitude upon the switching of applied bias. Furthermore, the piezoelectric coefficient was calculated from PFM, with a calculated d_{33} of 4.5 pm/V amplitude (note S4). This d_{33} value was almost consistent with the reported piezoelectric coefficient of PAN fibers. In addition to demonstrating the direct piezoelectric effect associated with the piezoelectric fibers, we fabricated a flexible test device composed of polymer-embedded piezoelectric fibers sandwiched between a copper top electrode and a conducting polyethylene terephthalate substrate. The voltage signals generated while periodically percussion and oscillation testing on the device further validated the theoretical piezoelectricity of the bio-NGs (Fig. 2K).

Physicochemical characterizations of bio-NGs

The piezoelectric conformation of the PAN-based fibers in bio-NGs was investigated by Fourier transform infrared (FTIR) and x-ray diffraction (XRD) spectra. The vibration bands at 1250 and 1230 cm^{-1} were assigned to zigzag conformation and 3^1-helical conformation of PAN, respectively (the inset of Fig. 3A and fig. S6), in which the planar zigzag conformation played a key role in piezoelectricity. On the basis of the FTIR spectra, the content of the zigzag conformation [$f(z)$] was estimated using Eq. 1

$$f(z) = \frac{A_{1250}}{A_{1230} + A_{1250}} \quad (1)$$

where A_{1230} and A_{1250} were the peak intensity at 1230 and 1250 cm^{-1}, respectively. The zigzag content of GO/PEDOT/Fe_3O_4/PAN fibers was 59.1%, which was comparable to PEDOT/Fe_3O_4/PAN fibers (59.3%) and slightly higher than Fe_3O_4/PAN fibers (58.6%) (Fig. 3C, blue columnar). The XRD patterns further confirmed the zigzag conformation in all PAN-based fibers (Fig. 3B, inset). The 2θ greater than 17° was attributable to the zigzag conformation in PAN conformation. In addition, Δθ = 2θ − 17 can be used to indicate zigzag conformation (*18*, *21*). As shown in Fig. 3C (red columnar), the 2θ of PAN-based fibers were all greater than 17°, indicating that the zigzag conformation in PAN-based fibers was dominant, matching well to FTIR results. Again, the high zigzag conformation content indicates high piezoelectricity of fibers in bio-NGs.

The thermodynamic properties of the piezoelectric PAN-based fibers in bio-NGs were analyzed by differential scanning calorimetry (DSC) thermogram. A weak exothermic peak at 110°C appeared in all DSC thermograms, which was the heat released by the crystals in PAN (Fig. 3D, inset). The crystallinity (X_c) can be calculated using Eq. 2

$$X_c = \frac{\Delta H}{\Delta H_f} \times 100\% \quad (2)$$

where X_c was the crystallinity of the sample, ΔH was the melting enthalpy of the sample, and ΔH_f (87.74 J/g) was the standard melting enthalpy of PAN with complete crystallization. As a result, the GO/PEDOT/Fe_3O_4/PAN fibers yielded the highest X_c value of 4.77%, while the X_c value of Fe_3O_4/PAN fibers was the smallest (3.22%). This indicated that the modification of PEDOT and GO was beneficial for improving piezoelectric performance. Besides, the melting temperature of PAN preoxidation shifted to a higher temperature from 301.01° to 317.07°C in GO/PEDOT/Fe_3O_4/PAN fibers, indicating that introducing PEDOT and GO can increase its thermal stability and thus hold long-term piezoelectricity in the body with higher temperature than ambient.

We further tested the charge storage and transmission properties of piezoelectric PAN-based fibers in bio-NGs using cyclic voltammogram (CV) (fig. S2B). Figure 3E showed that all PAN-based samples exhibited highly reversible CV profiles without any obvious side reactions (oxidation and reduction peaks), suggesting high electrochemical stability and that no reaction occurred in the bio-NGs. In addition, because of the high conductivity of PEDOT and the pseudo-capacitance effect of GO, GO/PEDOT/Fe_3O_4/PAN fibers yielded the highest charge capacity of 7.534×10^{-6}°C. This will facilitate the transmission of piezoelectric charges to the NG-cell interfaces and, thus, to promote the interaction between cells and ultimately modulate cell activity. In addition, the introduction of PEDOT and GO made the culture scaffold change from hydrophobic to hydrophilic, where the water contact angle decreased from 108 ± 3° to 84 ± 2° (Fig. 3F and fig. S3C). This hydrophilicity is almost the same as that of natural collagen fibers (*22*), indicating that our developed bio-NGs are conducive to cell adhesion and proliferation/growth.

To test the compressive resilience and mechanical properties of piezoelectric fibers assembled into bio-NGs, these fibers were fabricated into cylindrical shape with a diameter of 10 mm and a height of 10 mm (Fig. 3G, inset). We used a universal testing machine to compress the scaffolds, and the compression amounts studied are 5 mm (50%), 7.5 mm (75%), and 9 mm (90%), respectively. As shown in Fig. 3G, the fibers generally exhibited excellent resilience. When compressed by 50%, the rebound rate of the scaffolds was close to 100%. Even if compressed by 90%, the rebound rate of the scaffolds remained >93.33%; in particular, the target GO/PEDOT/Fe_3O_4/PAN fibers were as high as 98.44%. On the other hand, under the compression of 90%, the compressive modulus of these fibers modified by GO was notably increased up to 117 Pa, which was almost

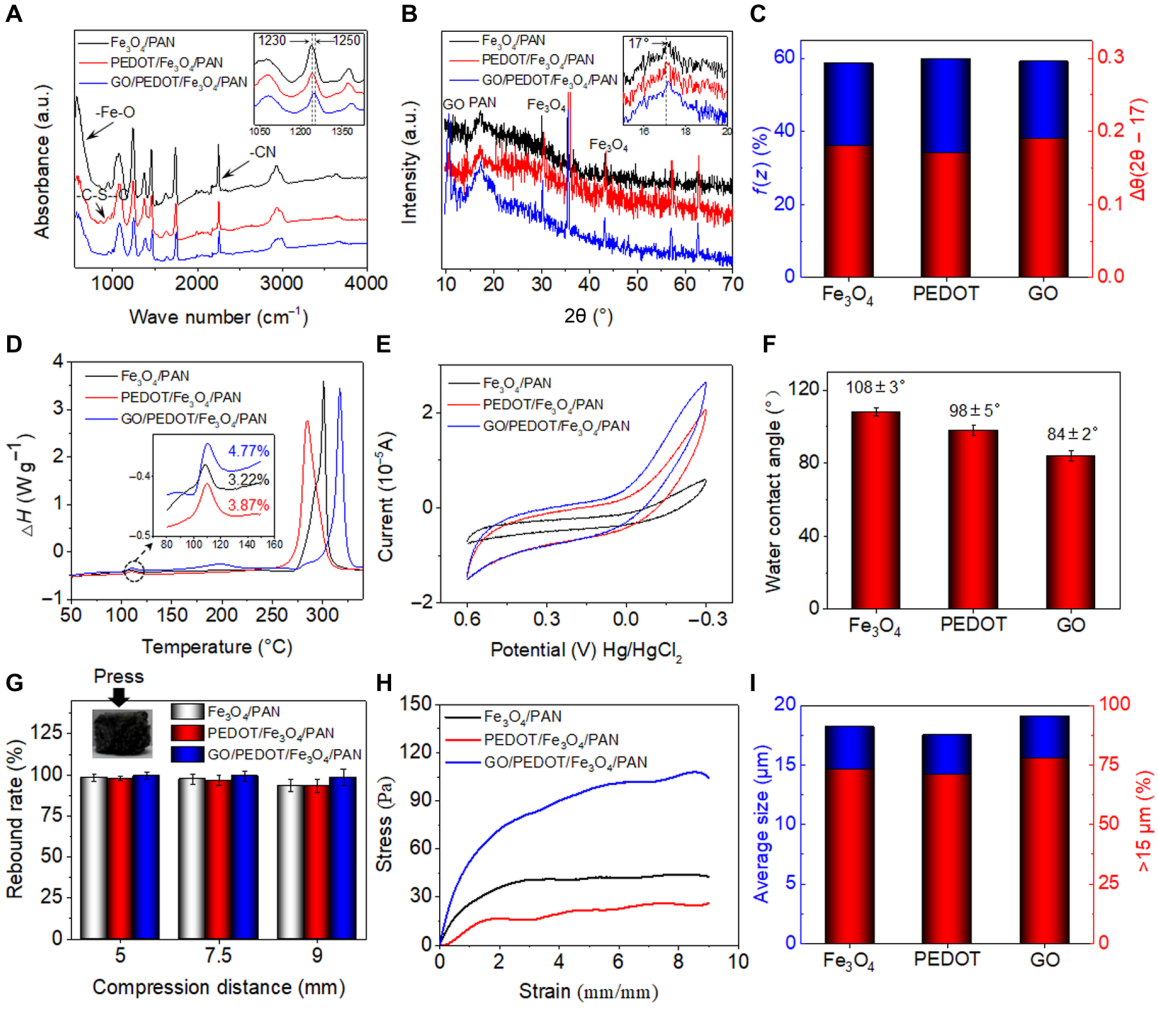

Fig. 3. Crystallinity and spatial structure stability characteristics of piezoelectric PAN-based fibers in bio-NGs. (**A**) FTIR and (**B**) XRD spectra of the Fe_3O_4/PAN, PEDOT/Fe_3O_4/PAN, and GO/PEDOT/Fe_3O_4/PAN fibers. a.u., arbitrary unit. (**C**) The content of the zigzag conformation and Δθ (2θ − 17) values of the Fe_3O_4/PAN, PEDOT/Fe_3O_4/PAN, and GO/PEDOT/Fe_3O_4/PAN fibers, quantified from the FTIR and XRD spectra, respectively. (**D**) DSC thermograms, (**E**) cyclic voltammogram (CV) profiles, and (**F**) water contact angle of the Fe_3O_4/PAN, PEDOT/Fe_3O_4/PAN, and GO/PEDOT/Fe_3O_4/PAN fibers. (**G**) Compression rebound rate of the Fe_3O_4/PAN, PEDOT/Fe_3O_4/PAN, and GO/PEDOT/Fe_3O_4/PAN fibers at 5-, 7-, and 9-mm compression. (**H**) Stress-strain curve of bio-NGs at 90% compression. (**I**) Average pore size distribution and the ratio of average particle size >15 μm. All error bars indicate ±SD. Photo credit: Chuanmei Shi, Nanjing University of Science and Technology.

three times of the Fe_3O_4/PAN fibers (Fig. 3H). Such excellent elastic modulus achieved the mechanical properties required in soft tissue cell culture (0.1 to 3 kPa) (*23*). These excellent resilience and mechanical properties ensured that bio-NGs composed of GO/PEDOT/Fe_3O_4/PAN fibers can effectively maintain their large enough pore size (>15 μm; Fig. 3I), thus providing a stable 3D growth microenvironment for cell movement and growth.

Cell activity regulation and its function maintenance via bio-NGs

The NG-cell interaction in 3D space was evaluated using two different cell lines: RGC5 cells and primary hepatocytes. The former presented voltage-gated calcium channels in their membranes, whereas the latter were motile cells with high metabolic functions. To fully evaluate the feasibility of 3D cell living space and NG-cell interaction as a live cell electrical stimulator, we used tissue culture plate (TCP), 2D NGs (note S5), and nonpiezoelectric 3D GO/PEDOT/Fe_3O_4/polylactic acid fibers (referred to as 3D fibers; note S6) as control substrates. Among them, TCP as a basic control group was used to evaluate the cytocompatibility of our bio-NGs. 2D NGs and nonpiezoelectric 3D fibers were used to evaluate the effects of 3D space and electrical stimulation on cells, respectively.

RGC5 cells with high electrical responsiveness were used to evaluate the potential neural induction of the bio-NGs. DNA assay was first performed to evaluate proliferation of RGC5 cells in bio-NGs. OD_{260} was the absorbance of the double-stranded DNA excited by the laser with a wavelength of 260 nm, which was used to count the relative number of cells. As shown in Fig. 4A, DNA tests showed that the number of RGC5 in the bio-NGs did not exhibit significant difference compared to the TCP in 5 days, suggesting cytocompatibility of bio-NGs. Next, we comprehensively evaluated the apoptosis of RGC5 cells cultured for 5 days. In the apoptosis diagram (Fig. 4B and fig. S7), Q1, Q2, Q3, and Q4 represented mechanical injury dead cells, nonviable apoptotic cells, normal cells, and early apoptotic

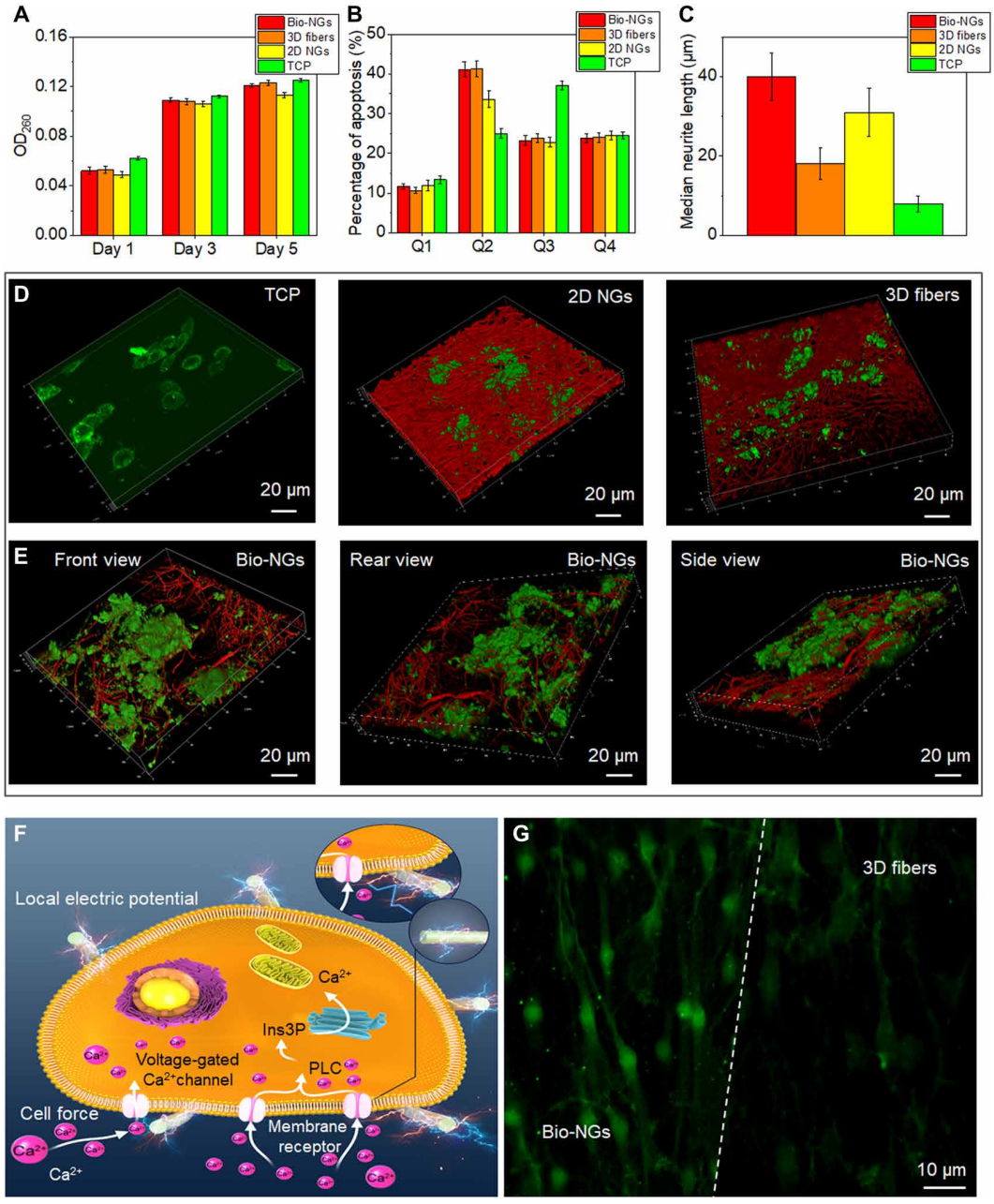

Fig. 4. The growth and development of RGC5 neurons in bio-NGs. (**A**) Proliferation of RGC5 neurons by the DNA assay on days 1, 3, and 5. (**B**) Apoptosis of RGC5 neurons after 5 days of culture in bio-NGs. (**C**) Neurite outgrowth of RGC5 neurons by the median neurite length after 5 days of culture in bio-NGs. (**D**) 3D confocal scanning of RGC5 neurons cultured on TCP, 2D NGs, and 3D fibers. (**E**) 3D confocal scanning of RGC5 neurons cultured in bio-NGs from different perspectives. (**F**) Inherent cell force of living cells grown in bio-NGs. This would induce a local electrical field proportional to the strain level that could eventually alter the membrane potential and/or the configuration of membrane receptors and results in the opening of the Ca^{2+} channels. Ins3P, inositol trisphosphate. PLC, phospholipase C. (**G**) The fluorescence images of the cells preincubated with Fluo-4 AM (membrane-permeable and Ca^{2+}-dependent dye) on the fibers in bio-NGs and 3D fibers. Green, Ca^{2+}. All error bars indicate ±SD.

cells, respectively. We found that the Q1 value (11.71%) and Q4 value (23.91%) of the cells in bio-NGs both were lower than those of TCP (Q1: 13.42%; Q4: 37.1%), indicating that bio-NGs did not affect the cell cycle. Notably, the Q2 value of bio-NGs (41.16%) was significantly greater than that of TCP (25.0%), while the Q2 value (38.61%) of 2D NGs prepared with the same materials as the bio-NGs was significantly reduced. The advanced apoptotic cells in bio-NGs were mainly caused by too many cells to effectively exchange metabolites and nutrients with the culture medium. This was further confirmed by the Q2 value (41.28%) of 3D fibers. These data again confirmed that bio-NGs were able to be used to provide a bio-friendly cell culture microenvironment.

Next, cell adhesion to the bio-NGs was assessed, as this was a key parameter for the induction of the piezoelectric effect (*20*, *24*). The

intracellular tension can be transmitted, via focal contacts, to the underlying substrate (*25*–*27*). Consequently, if a cell firmly adheres to the surface of piezoelectric fibers, then any inherent forces produced by this cell will result in the generation of an electric field near the cell plasma membrane. To better observe the interaction between cells and bio-NGs, bio-NGs and RGC5 cells were stained with the fluorescent agent rhodamine B and the live cytoskeleton fluorescent dye calcein-AM, respectively. When performing 3D confocal scanning, the adhesion state between the NGs and the cells can be observed by simultaneously exciting the rhodamine B (red) and calcein-AM (green). These cells tightly adhered to and wrapped on the fibers in bio-NGs from multiple view angles (Fig. 4E) but only grew on the surface of the 2D NGs (Fig. 4D, middle). Although the spatial structure of 3D fibers (fig. S8) was similar to that of bio-NGs, local cell aggregates were still distributed in the 3D fibers in a sheet-like distribution [Fig. 4D (right) and fig. S9]. This might be because the electric potential existed at the NG-cell interface, which promoted the cells to produce many pseudopodia and, thus, to better adhere to the NGs. This piezopotential yielded by bio-NGs accelerated cell neuraxonization, as confirmed by the median neurite length of RGC5 cells (fig. S10). As shown in Fig. 4C, the median neurite length of bio-NGs was the longest, as high as 40 μm, while the median neurite length of 3D fibers was only 18 μm. Despite this, the median length of neurites on 2D NGs (31 μm) was 1.72 times longer than that of 3D fibers. Therefore, these results suggested that the electromechanical interaction with NGs can accelerate the development of neuronal cells.

Last, we analyzed changes in intracellular calcium concentration (Ca^{2+}), induced by the cell-NG interaction. It is well known that RGC5 cells exposed to an electrical field can undergo changes in their cytosolic Ca^{2+} (*3*, *28*). Ca^{2+} was a secondary messenger involved in multiple signal transduction pathways. The Ca^{2+} in the cytosol of resting cells was extremely low, but when signaling was activated, a large increase occurs. Several factors can induce the intracellular calcium increase, such as growth factors (*29*) or electrical stimulation (*30*–*32*). Voltages able to locally change the membrane potential would trigger the opening of voltage-gated calcium channels (Fig. 4F), allowing an influx of extracellular Ca^{2+} that would activate the calmodulin kinases. To verify this, the Ca^{2+}-dependent dye Fluo-4 AM was used to fluorescently stain the RGC5 neurons in bio-NGs and nonpiezoelectric 3D fibers, respectively, in which the fluorescence intensity could express the intracellular Ca^{2+} concentration to a certain extent. Compared with 3D fibers, the cells in bio-NGs showed stronger Ca^{2+} expression (Fig. 4G). These results suggested that cell adhesion forces were able to shock or bend the fibers in bio-NGs, inducing the generation of a local electric field large enough to stimulate the cells and alter their activity.

It is well known that electric potential can stimulate and regulate the movement of motile cells (*33*, *34*). Here, primary hepatocytes were selected as exemplary motile cells to evaluate the bio-NG–cell interaction. We first used a light microscope to intermittently record the hepatocyte motility at hour 3, day 1, and day 3. As shown in Fig. 5A, after 3-hour cell seeding, the attached hepatocytes in bio-NGs remained separate. In the following culture time, hepatocytes in bio-NGs started to move together and lastly formed spheroid hepatocyte aggregates with diameter of ~60 μm. Then, the state of hepatocytes cultured for 3 days was further carefully observed by scanning electron microscopy (SEM). Each aggregate in bio-NGs was composed of multiple single hepatocytes (Fig. 5B). Most of hepatocytes on 3D fibers also formed spheroid aggregates, but their diameters were generally smaller than 30 μm (fig. S11B). As for 2D NGs, some hepatocytes formed sheet-like aggregates (diameter, 10 to 60 μm), but many hepatocytes did not inosculate into these aggregates (fig. S11C). Cell motility was further evaluated by counting hepatocyte aggregate size and number. After 3 days in culture, we randomly chose and observed 10 areas on each sample with an inverted microscope and manually recorded the number of hepatocyte aggregates (diameter, >25 μm) and the average diameter of hepatocyte aggregates (Fig. 5C). Bio-NGs and 3D fibers had similar aggregate numbers of hepatocytes with a diameter greater than 25 μm, which was much higher than that of TCP and 2D NGs. This suggested that fibers in 3D space could provide stress support for hepatocytes and induce their migration to form aggregates. However, the aggregate size in bio-NGs was the largest of 60 μm (average diameter), which was 2.1 times that of 3D fibers (28 μm), indicating that cell-NG interaction could promote long-distance migration of hepatocytes. This was further proved by 2D NGs. Although fewer aggregates formed on 2D NGs, the average diameter of aggregates also still reached 40 μm. Comprehensively considering the number and size of aggregates, it is concluded that the electromechanical cell-NG interaction in 3D space can further improve cell mobility and facilitate long-distance displacement.

Next, the adhesion of cells to the NGs after a 3-day culture was evaluated by SEM. We observed that the membrane of cells cultured in bio-NGs was in close contact with the fibers and that those cells emitted short and long projections (i.e., pseudopods) firmly attached to piezoelectric fibers in bio-NGs (Fig. 5, D to F). The ECM secreted by the cells completely covered the fibers, further indicating that bio-NGs had excellent fusion with cells. Such close adhesion between the cells and NGs can drive NGs to yield local potential on the cell membrane. To observe the cell-NG interaction more clearly, the primary hepatocytes were stained with calcein (green), a fluorescent dye related to intracellular calcium density and circulation. Calcein staining image showed the presence of overexpressed cell matrix between cells (bright green) as shown in Fig. 5H, which was caused by fusion between cells, suggesting that the cells in aggregates had abundant information exchange. Furthermore, thanks to the continuous 3D fiber structure, different cell aggregates could also exchange information with each other (Fig. 5G). These data confirmed that the 3D growth space and NG-cell interaction coordinated to drive cell migration and reunion and eventually form widespread cell clusters with similar cell morphology to natural hepatic tissue.

As we previously reported, cell aggregation can help maintain the viability and hepatic function expression of primary hepatocytes (*35*, *36*). First, 3-(4,5-dimethylthiazol-2yl)-2,5-diphenyl-2*H*-tetrazolium bromide (MTT) assay was performed to evaluate the cellular metabolic activity. As shown in Fig. 5I, MTT tests showed that the hepatocytes on fiber-based culture scaffolds displayed better cell activity overall than those on TCP; in particular, the hepatocytes in bio-NGs displayed good cell viability even after 15 days of culture. This was because broad cell aggregates existed in bio-NGs, while most of the hepatocytes on TCP were rounded, separated, and had little cell-cell contact (fig. S11A). Then, albumin (Alb) secretion was selected as a reference for assessing hepatic function maintenance since the production of Alb was the main synthetic function of hepatocytes. As shown in Fig. 5J, hepatocytes cultured in bio-NGs expressed the highest level of Alb secretion. From days 1 to 7, the Alb secretion of

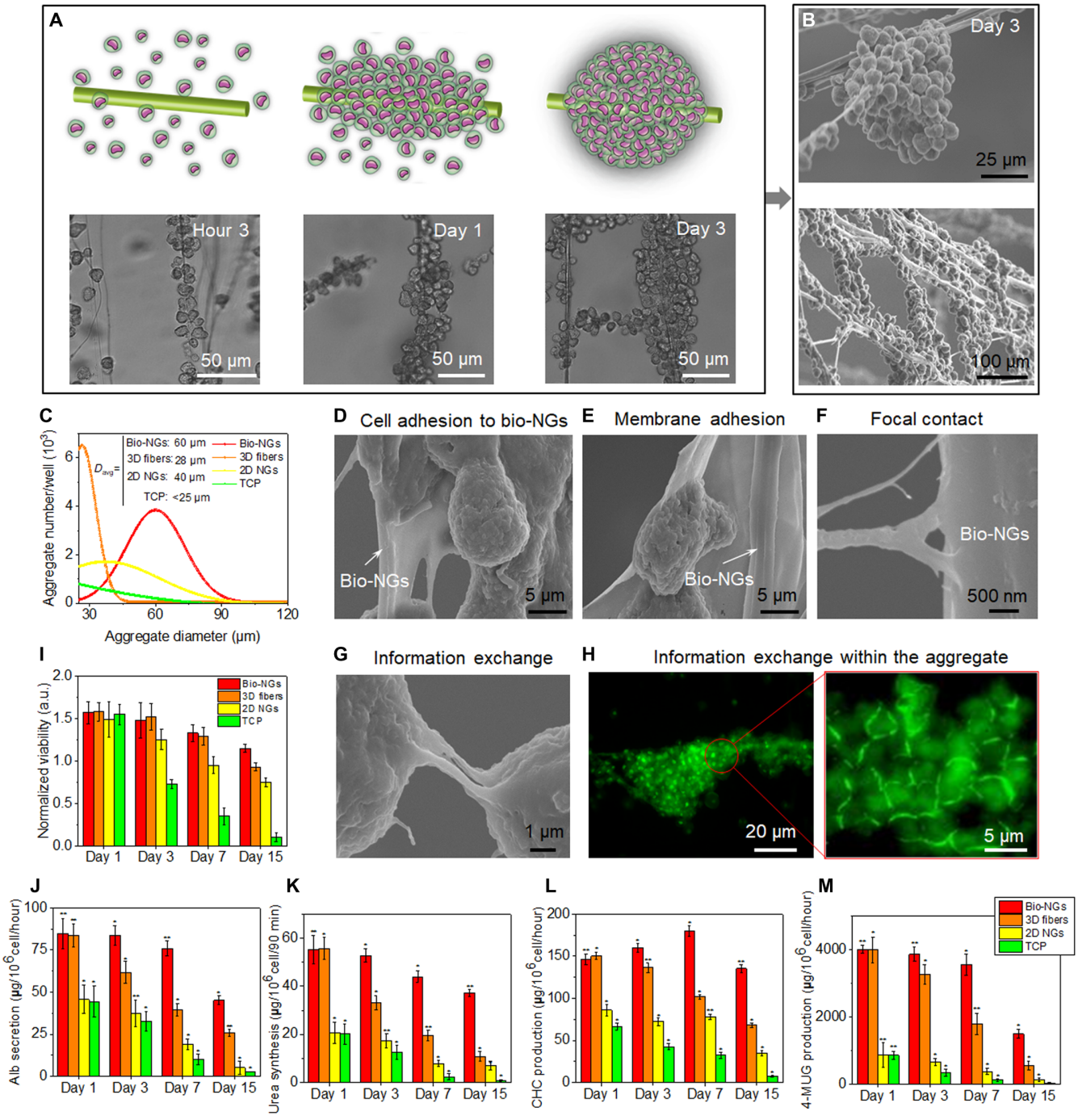

Fig. 5. The motility and function maintenance of primary hepatocytes in bio-NGs. (**A**) Schematic diagram and light microscope images of hepatocyte movement to form cell clusters. (**B**) SEM images of hepatocyte aggregates. (**C**) Hepatocyte aggregate size and number on day 3. (**D** to **F**) Cell morphology and NG-cell interaction including cell membrane adhesion and focal contact, assessed by SEM after 15 days in culture, showed that hepatocytes were adhered to fibers in bio-NGs. (**G**) SEM image showing the information exchange between cell aggregates. (**H**) Laser scanning confocal microscopy images of epithelial cadherin (green) detection showing the cellular information exchange within cell aggregates. (**I**) MTT assay showing no signs of toxicity for cells cultured in bio-NGs. Hepatic function assessment: (**J**) Albumin (Alb) secretion and (**K**) urea synthesis at different culture time points. The metabolic functions of hepatocytes: (**L**) 3-cyano-7-hydroxycoumarin (CHC) and (**M**) 4-methylumbelliferyl glucuronide (4-MUG) production at different culture time points. All error bars indicate ±SD. $n = 3$. $^{*}P < 0.05$ and $^{**}P < 0.01$.

hepatocytes cultured in bio-NGs decreased slightly (day 1: 84.7 μg; day 7: 75.9 μg), while from days 7 to 15, a rapid decline in Alb secretion from 75.9 to 45.1 μg occurred. This might be because of the death of free hepatocytes and the inevitable damage in the process of cell isolation. Unlike bio-NGs, the Alb secretion of hepatocytes cultured in 3D fibers continued to drop sharply from day 1. This indicated that the local voltage potential yield by NGs was beneficial to functional stability of hepatocytes. On the other hand, the Alb secretion

of hepatocytes cultured in 3D scaffolds including bio-NGs and 3D fibers was significantly higher than that of the 2D scaffolds (i.e., TCP and 2D NGs), suggesting that 3D space was important for the functional maintenance of hepatocytes. Similar patterns were also found in urea synthesis (Fig. 5K). Accordingly, 3D growth space and NG-cell interaction can coordinate to maintain and prolong the functional stability of hepatocytes. Cytochrome P-450 1A (CYP1A; phase I metabolic enzyme) and uridine diphosphate–glucuronyltransferase (UGT; phase II metabolic enzyme) enzymatic activity stimulated by 3-cyano-7-ethoxycoumarin (CEC) and 4-methylumbelliferone (4-MU), respectively, were used to evaluate metabolic functions of hepatocytes. Hepatocytes cultured in 3D scaffolds displayed a significantly higher conversion rate of CEC to 3-cyano-7-hydroxycoumarin (CHC) than those on 2D scaffolds throughout the entire culture period (Fig. 5L), indicating that the 3D cell growth space can increase the CYP1A enzymatic activity. The highest CYP1A enzymatic activity appeared on day 7 because of the formation of large cell monolayers and the subsequent recovery of hepatic function by the hepatocytes in bio-NGs. Different from the bio-NGs, the highest CYP1A enzymatic activity of hepatocytes cultured in 3D fibers appeared on day 1 and then continued to decline. These values were generally lower than those of bio-NGs, which indicated that local potential could promote the phase I metabolism of hepatocytes. A similar trend in UGT enzymatic activity assessment was observed (Fig. 5M), suggesting that 3D growth space and NG-cell interaction also benefited the phase II metabolism of hepatocytes.

In addition, hMSCs were selected as another group of cell lines to further confirm this bio-NG–cell interaction (fig. S12 and note S7). Electric stimulation is well recognized as an effective method to elicit osteogenic differentiation of stem/progenitor cells and bone formation (*37*). To clearly observe the differentiation morphology of the cells, hMSCs were fluorescently stained with fluorescein diacetate (FDA). The hMSCs displayed spindle-shaped morphology, especially on 3D fibers and bio-NGs. In parallel, hMSCs cultured in 3D scaffolds including bio-NGs and 3D fibers exhibited a higher level of cell spreading. From the magnified view of the FDA fluorescent staining images, bio-NGs induced cell attachment with a more spread morphology compared to the other scaffolds (i.e., TCP, 2D NGs, and 3D fibers). Such a flattened and polygonal-shaped morphology of hMSCs in bio-NGs, analogous to the features of osteoblasts, indicated the early onset of differentiation. To confirm this osteoblastic differentiation, the activity of alkaline phosphatase (ALP), one of the early osteogenic markers, was evaluated. Almost at each time point studied, the ALP activity (the early osteogenic markers) of hMSCs was significantly higher in bio-NGs, when compared to the other scaffolds (i.e., TCP, 2D NGs, and 3D fibers). Again, this further proved that the 3D space coupled with NG-cell interactions promoted the differentiation of osteoblasts. Together, the bio-NG–cell interactions can maintain and prolong the specific functional expression, which is expected to be applied to cell/tissue engineering research and potential therapeutic applications, such as bioartificial liver devices, nerve injury repair, liver injury repair, etc.

Liver repair promotion by bio-NGs in vivo

As an exemplary demonstration, the bio-NGs were implanted into the area of liver injury (Fig. 6A). This region related to hepatocyte regeneration echoed the above-mentioned primary hepatocyte culture in vitro, which could be used to reflect the real-world practicality of bio-NGs. For animal clinical research, Sprague-Dawley rats were used as standard model animals. We removed a cylindrical liver tissue with a diameter of 10 mm and a height of 6 mm from the middle part of the third lobe liver, resulting in acute liver injury. The implants were taken out after 1, 2, and 4 weeks of implantation. Inflammation analyses were performed by staining prepared tissue slides from the liver around bio-NGs with hematoxylin and eosin (H&E). Mild inflammation was found in the first week, which was improved from the second week, and reduced to the normal level at week 4 (Fig. 6, B and D). Synchronously, pathological tests were also conducted on most vital organs, including heart, lung, kidney, and brain. H&E staining was collected from these organs at different time points (weeks 1, 2, and 4) after implantation. All the organs showed no deformation and abnormal lymphatic cell invasion (fig. S13), which further confirmed that all the rats were in a good health condition, and bio-NGs had no systemic side effects. On the other hand, acute liver injury was usually accompanied by liver fibrin(ogen) deposition that played a key role in the process of coagulation and hemostasis. Large-scale fibrin(ogen) deposition occurred in the first week and then returned to a normal level at week 4 (Fig. 6, C and E). This indicated that a new blood circulation system (i.e., blood vessel) was formed inside the regenerated liver tissues. Notably, compared with bio-NGs, even after 4 weeks of implantation, the tissue regenerated in 3D fibers still showed slight inflammation and blood barriers (fig. S14). Such data suggested that bio-NG–cell interactions could alleviate inflammation and promote tissue repair. This was consistent with other reported conclusions that electric stimulation can minimize inflammation and accelerate angiogenesis (*38*).

Next, immunostaining for Alb was used to evaluate the expression level of hepatic function in the regeneration area. As shown in Fig. 6F, it could be seen intuitively that both the density of regeneration cells (blue) and the level of Alb secretion (red) in bio-NGs increased with the implantation time. To quantify this expression level, we extracted the percentage of the area with Alb expression as shown in Fig. 6G. From weeks 1 to 4, Alb secretion level increased significantly, indicating more hepatocyte generation in this region. In contrast, the expression level of Alb in the regenerated tissue in 3D fibers was significantly weaker than that in bio-NGs (fig. S15), matching well to the conclusions obtained from in vitro primary hepatocyte culture. It has been proposed that hepatocytes in all three zones (i.e., periportal zone, central zone, and midzonal) contributed to liver homeostasis or regrowth after injury or disease (*39*, *40*). To deeply evaluate the performance of the regrowth liver, we further studied the regenerated hepatocytes in these three distinct zones. The periportal zone surrounding the portal vein was marked by E-cadherin (E-CAD), which was defined as zone 1, while the central zone nearest to the central vein labeled as zone 3 was immunostained by glutamine synthetase (GS). As for zone 2, it was composed of the midzonal hepatocytes in between zones 1 and 3 (Fig. 6H). It could be found that proliferating periportal hepatocytes gradually streamed toward the central vein, where they were eventually eliminated (Fig. 6, I and J), suggesting good liver function expression, which was well matched to a typical hepatocyte streaming model with its portal-to-central directionality (*41*). However, this phenomenon was not found in the 3D fibers of the comparison group (fig. S16). This indicated that bio-NGs effectively accelerated the repair of the liver. On the other hand, E-CAD expression was restricted to periportal hepatocytes, while, in perivenous hepatocytes, GS was expressed. Therefore, both E-CAD and

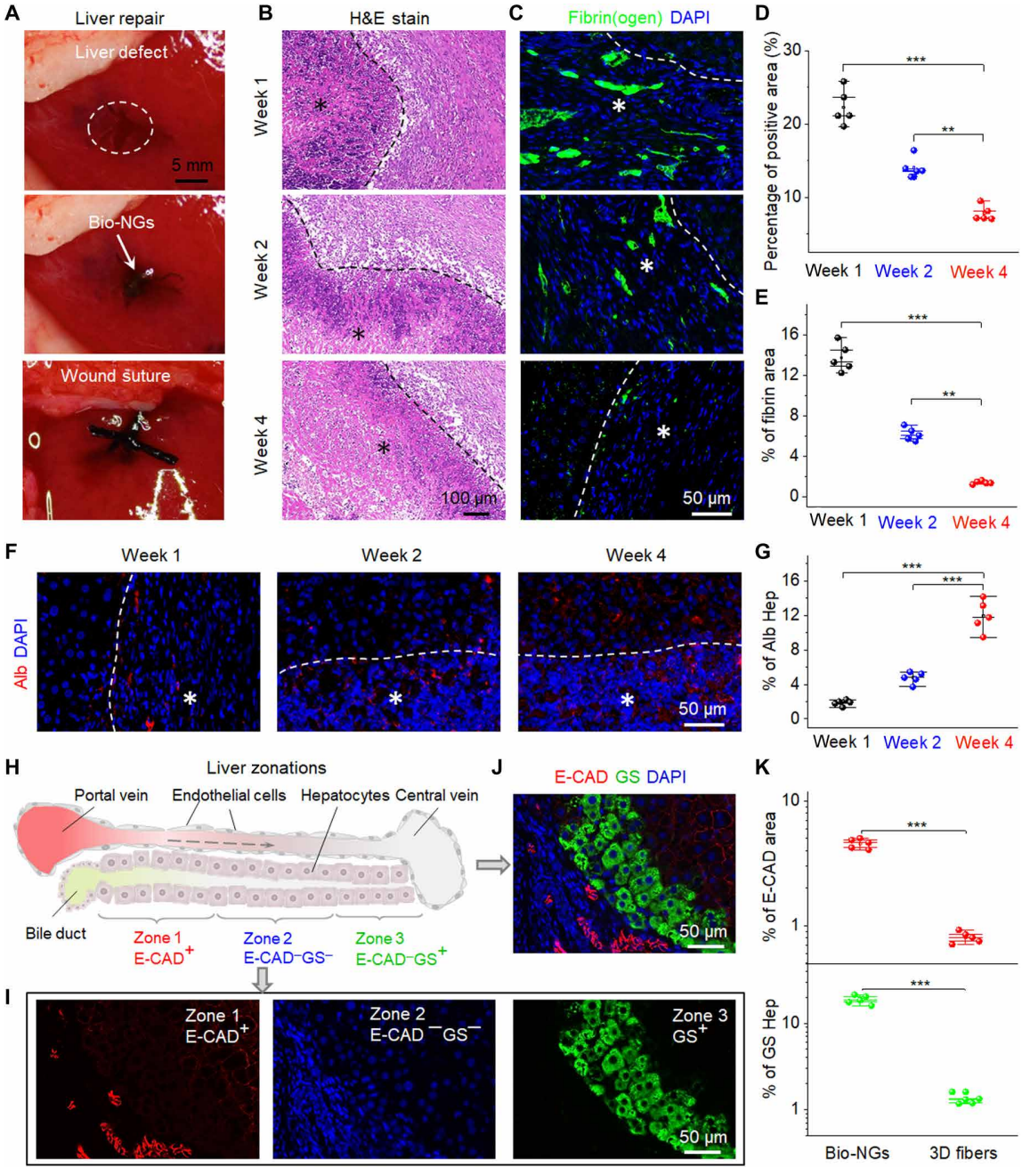

Fig. 6. Liver repair promotion by bio-NGs in vivo. (**A**) Surgical images showing the implantation of the bio-NGs into the liver defect. (**B**) H&E staining of the liver sections at different time points (weeks 1, 2, and 4) after implantation. (**C**) Representative images of hepatic fibrin(ogen) immunostaining (green) in 4′,6-diamidino-2-phenylindole (DAPI) (blue)–counterstained liver sections at the implanted area. (**D**) Average percentage of the positive area measured from H&E staining. (**E**) Quantification of hepatic fibrin immunofluorescent labeling. (**F**) Immunostaining for Alb (red) on liver sections at different time points (weeks 1, 2, and 4) after implantation. (**G**) Alb expression level measured from Alb immunostaining. (**H**) Schematic showing three liver zones from the periportal to the pericentral region. 1, 2, and 3 indicate zone 1 ($E\text{-}CAD^{+}$), zone 2 ($E\text{-}CAD^{-}GS^{-}$), and zone 3 (GS^{+}), respectively. The dashed arrow indicates blood flow. (**I** and **J**) Immunostaining for GS (green) and E-CAD (red) on liver sections at the fourth week after implantation. (**K**) Quantification of GS and E-CAD showing stronger expression of liver function of new hepatocytes in bio-NGs than that of 3D fibers. Hep, hepatocyte. Asterisks (*) show locations of the implantation. Data are expressed as mean values ± SD. $n = 5$. $^{**}P < 0.01$ and $^{***}P < 0.001$. Photo credit: Fei Jin, Nanjing University of Science and Technology.

GS expression levels could also be used to evaluate the blood vessels in the regenerated liver and then indirectly reflect the blood flow inside. Obviously, the expression levels of E-CAD and GS in regenerated tissues in bio-NGs were almost an order of magnitude higher than that of 3D fibers (Fig. 6K), matching well to the results obtained by fibrin(ogen) immunostaining, which indicated that bio-NGs could accelerate the formation of blood vessels. As a result, all the data suggested that bio-NG–cell interactions were also applicable in vivo, which could coordinate to accelerate liver repair and maintain its specific functional expression.

Long-term in vivo stability and biocompatibility of bio-NGs

The NG-cell interaction in 3D space was proven to efficiently promote cell viability and maintain its functional expression in vitro and in vivo, which provided a treatment strategy for clinical trials including nerve defects (i.e., acoustic nerve, optic nerve, etc.) and permanent cell damage (i.e., cardiomyocytes, skeletal muscle cells, etc.). For such diseases, nerve defects, or tissues/cells that were difficult to regenerate in the body, the most effective method was to directly transplant functional cells to the damaged site in vivo (*42*–*46*). The cell-scale in situ 3D electrical stimulators that we constructed can be well qualified for culturing such functional cells. To further demonstrate the real-world application potential in vivo, the bio-NGs were implanted into the gastrocnemius muscle area and around the sciatic nerve of the rats (Fig. 7, A and B). These regions were associated with greater muscle rhythmicity, which could diagnose the potential infections and necrosis in surrounding tissues and evaluate the mechanical stability of the bio-NGs in vivo. The implants were taken out after 1, 2, 4, and 8 weeks of implantation. Inflammation analyses were performed by staining prepared tissue slides from the gastrocnemius muscle area and sciatic nerve with Masson and tumor necrosis factor–α (TNF-α), respectively. The histological images of the implantation area showed a very mild immune reaction without notable presence of inflammation and cellular toxicity (Fig. 7C). Mild fibrosis and activated macrophages were found in the first week, which was improved from the second week, and reduced to the normal level at week 4 (Fig. 7E). A similar trend in TNF-α assessment of the sciatic nerve was observed from Fig. 7 (D and F). Besides, the bio-NG implanted for 8 weeks was wrapped by surrounding muscle or nerve tissue, with no tissue ulceration occurrence, and still maintained its stable 3D structure (fig. S17). These data showed that the bio-NGs had good biocompatibility and could maintain stable performance over a long time in biological environment. Last, we also performed pathological tests on most vital organs at week 8 after implantation, including liver, heart, lung, kidney, and brain. No deformation and abnormal lymphatic cell invasion occurred in these organs (Fig. 7G), indicating that the bio-NGs had no systemic side effects. Together, they are promising to be used as implants, bearing functional cells to be implanted into diseased parts of the body.

DISCUSSION

In this work, we developed ECM-like electromechanical coupling bio-NGs that can modulate cell activity and maintain its specific

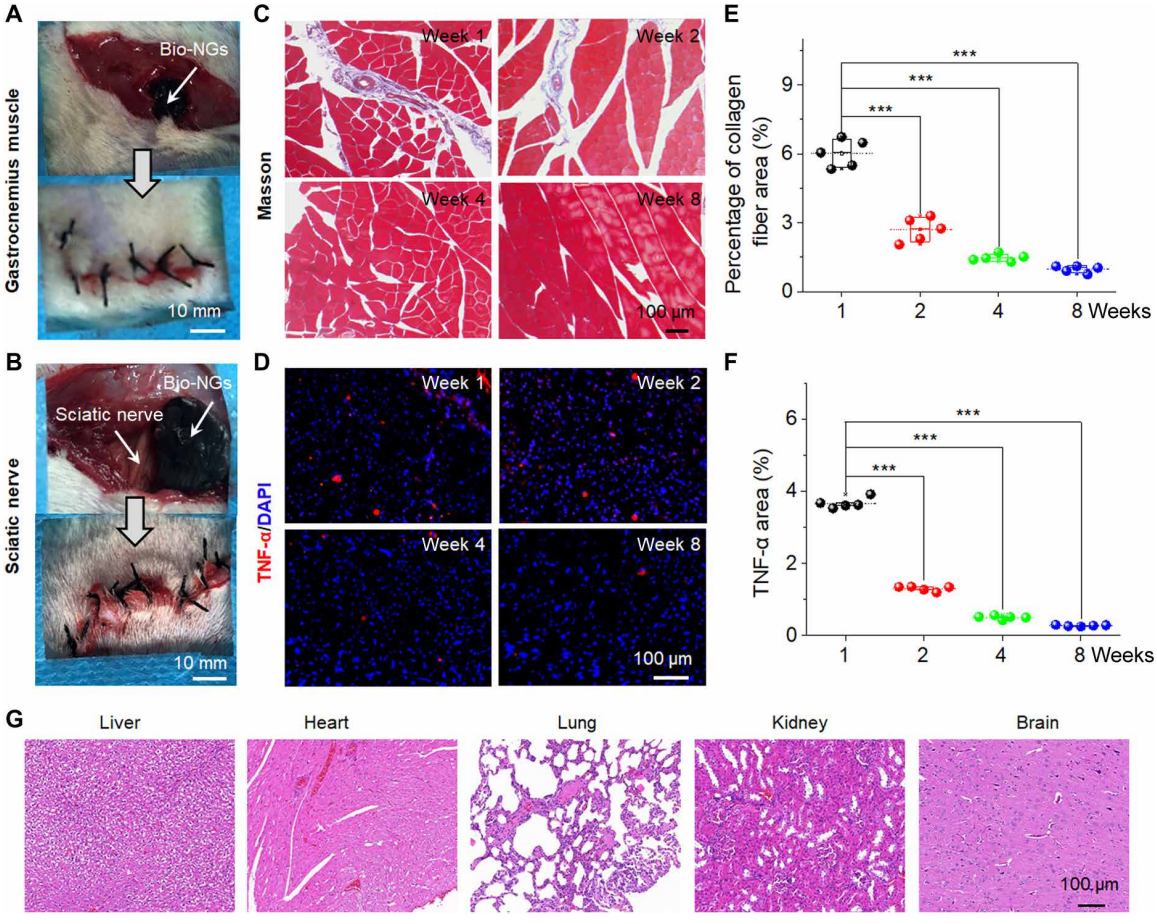

Fig. 7. In vivo stability and biocompatibility of bio-NGs. Surgical image showing the implantation of the bio-NGs into the (**A**) gastrocnemius muscle and (**B**) sciatic nerve areas of a mouse. (**C**) Masson trichrome staining of gastrocnemius muscles at the implanted area. (**D**) TNF-α immunofluorescent staining of sciatic nerve at the implanted area. (**E**) Average percentage of collagen fibers in the muscle tissue measured from Masson staining. (**F**) Relative TNF-α expression level measured from TNF-α immunofluorescent staining. (**G**) H&E staining of vital organs (liver, heart, lung, kidney, and brain) at week 8 after implantation in the sciatic nerve area. Data are expressed as mean values ± SD. $n = 5$. ***$P < 0.001$. Photo credit: Tong Li, Nanjing University of Science and Technology.

functional expression. The traction force of living cells in bio-NGs can induce the deformation of piezoelectric fibers, thus creating a local voltage potential. The local voltage potential near the cell membrane would provide continuous electric stimulation for the living cells as long as the cells were under movement and traction. In addition, the unique 3D space and in situ electrical stimulation provided an ECM-like growth microenvironment for cells, which was conducive to the correct expression of functional cells including cell phenotype and specific expression. As a result, when cells were cultured in bio-NGs, the NG-cell interactions in 3D space triggered the opening of ion channels present in the plasma membrane of RGC5, inducing intracellular calcium transients, and stimulated the motility of primary hepatocytes to form broad cell aggregates, as well as accelerated the differentiation of hMSCs into osteoblasts. Besides, it was verified that the 3D cell growth space and NG interaction can promote cell viability and development and maintain its specific functional expression (i.e., neuraxonization of RGC5 and special liver function of primary hepatocytes). Different from traditional probe-type electrical stimulation that applied external electrical pulses to an undetermined group of cells, our bio-NGs provided a strategy to achieve single cell–level electrical stimulation. Such in situ cell-scale electrical stimulation in 3D space can be widely extrapolated to other excitable functional cells, such as glandular or muscle cells, offering great potential for future bioelectronic medicines based on cell-targeted local electrical impulses.

To evaluate the practicality of in vivo applications, we chose the liver as the implantation point that echoed the above-mentioned primary hepatocyte culture in vitro. In this way, it was convenient to analyze the effect of bio-NG–cell interactions on cell regulation and its function maintenance in vitro and in vivo. We found that the expression level of liver function in the regenerated tissue in 3D fibers was significantly weaker than that in bio-NGs, matching well to the conclusions obtained from in vitro primary hepatocyte culture. Notably, this bio-NG–cell interaction was also applicable in vivo, which could reduce inflammation, induce hepatocyte proliferation, and accelerate angiogenesis inside the regenerated tissues, thereby ultimately promoting liver repair. This could be explained by the mechanism by which electrical stimulation promoted tissue repair within three intersecting stages (i.e., inflammation, proliferation, and remodeling) disclosed in recent studies (*38*, *47*, *48*). In the inflammation stage, electrical stimulation can increase blood flow and tissue oxygenation supply to inhibit bacterial growth and minimize inflammation. In the proliferative phase, electrical stimulation accelerated wound contraction, functional cell proliferation, angiogenesis, and collagen deposition. In the remodeling stage, electrical stimulation enhanced maturation and remodeling of collagens, thereby accelerating tissue repair from injury or defect. Therefore, the electrode-less and battery-free methods for in situ electrical stimulation on cells in 3D space provided unlimited possibilities for future bioelectronic therapies, where controlled electrical impulses can replace the use of chemical drugs for disease treatment, nerve/tissue repair, and regeneration.

Many diseases including nerve defects and permanent cell damage were difficult to regenerate/repair in the body; the most effective method was to directly transplant matched functional cells to the diseased site in vivo (*42*–*46*). Since our bio-NGs can effectively promote cell viability and maintain its functional expression in vitro and in vivo, this provided a treatment strategy for clinical trials of such diseases. Here, we took heart failure caused by the loss of cardiomyocytes as an example to carry out an in-depth discussion. Heart failure was the leading cause of death in most industrialized countries and a growing cause of death in emerging countries (*49*). The most common cause of heart failure was myocardial infarction (MI), which was a loss of myocardium because of oxygen and nutrient deficiency and replacement with noncontractile scar tissue. A primary challenge in developing therapies for cardiac muscle repair was the limited regenerative capacity of the myocardium (*50*). Currently, the only long-term treatment available to restore cardiac function after MI-related heart failure was heart transplantation. However, many patients died while waiting for a donor heart because of limited organ availability. Relevant studies showed that cardiac tissue engineering and cell-based therapies, represented by direct cell injection, were potential approaches for treating heart failure (*51*). Stem cells can be efficiently differentiated into cardiomyocytes for transplantation by electrical stimulation (*52*). The cell-scale in situ 3D electrical stimulation that we constructed can be well qualified for culturing such functional cells for transplantation in vivo. Notably, our bio-NGs showed good biocompatibility and had no systemic side effects and could maintain stable performance over a long time (>8 weeks) in biological environment. This offered an extraordinary building block for the implantation of bio-NGs bearing functional cells into the diseased site.

In summary, this advanced bio-NG that we developed is expected to fill the gap between the inaccurate 2D systems and the expensive and time-consuming animal models, mimicking the complexity of the ECM and the physiological relevance of an in vivo biological system. More broadly, the concept of this work on mimicking the bioelectrical signals generated from ECM showed a great potential for bioinspired bioelectronic medicine.

MATERIALS AND METHODS

Fabrication of bio-NGs

We fabricated bio-NGs in three steps. First, highly discrete Fe_3O_4/PAN fibers were fabricated by electrospinning the mixed solution of PAN (molecular weight, 40,000; Binzhou Hengtai Chemical Fiber Co. Ltd.) and Fe_3O_4 (99.9%; Sigma-Aldrich). With the introduction of Fe_3O_4 magnetic nanoparticles, 3D scaffolds with micropore that was suitable for cell migration can be prepared by electrospinning and received by water with assistance of magnetic field; besides, Fe_3O_4 could be relatively uniformly dispersed in the fibers. After the electrospinning, the prepared fibers were transferred into a 50-ml centrifuge tube and freeze-dried for 60 hours to obtain 3D Fe_3O_4/PAN scaffolds. Second, PEDOT was polymerized in situ on Fe_3O_4 PAN fibers. The freeze-dried Fe_3O_4/PAN fibers were soaked in diethyl ether (AR, Sinopharm Chemical Reagent Co. Ltd.) solution of EDOT (99%; Shanghai Aladdin Biochemical Technology Co. Ltd.) and $FeCl_3$ (99.9%; Shanghai Aladdin Biochemical Technology Co. Ltd.). The in situ polymerization process was performed under ultrasonic ice water bath. Third, GO (Nanjing Pioneer Materials Nano Technology Co. Ltd.) was introduced on PEDOT/Fe_3O_4/PAN fibers by electrostatic adsorption. The surface of GO was rich in anionic groups such as carboxyl and hydroxyl groups, which can be electrostatically adsorbed with PEDOT, thereby self-assembled into the GO outer layer. These GO/PEDOT/Fe_3O_4/PAN fibers acted as bio-NGs for cell culture. For more details, please see note S1.

Characterizations

The piezoelectric conformation in PAN was characterized by FTIR (Nicolet iS10, Thermo Fisher Scientific) and XRD (D8 Advance, Bruker).

The thermodynamic properties of the piezoelectric PAN-based fibers were analyzed by DSC (DSC-823E, Mettler Toledo). The morphology and structural distribution were observed by SEM (Supra 55, Carl Zeiss) and transmission electron microscopy (JEM-2100, JEOL). Water contact angle was tested by the contact angle measurement (XG-CAMB1, XUANYI). The resilience and mechanical properties of bio-NGs were measured by a universal testing machine (UTM2303, Jinan Kesheng Experimental Equipment Co. Ltd.). The output voltage was collected by an electrochemical workstation (CHI 760e). The piezoelectricity of the single fiber in bio-NGs was characterized by PFM (MultiMode 8, Bruker).

Cell cultured in bio-NGs

The experiments were divided into four groups, namely, TCP and 3D fibers and 2D NGs and bio-NGs. The samples were soaked in 75% alcohol for 30 min and washed four times with phosphate-buffered saline (PBS) buffer, then sterilized by ultraviolet (UV) light irradiation for 4 hours, and transferred to the 48-well culture plates.

RGC5 cells were used to evaluate the bio-NG–cell interaction that can trigger the opening of ion channels. RGC5 cells (50 μl) were seeded onto the samples at a density of 10^4 cells/ml in each sample with Dulbecco's modified Eagle's medium (DMEM) culture medium [10% fetal bovine serum (FBS), 1% penicillin, 1% glutamine, and 0.01% fungizone]. Then, the plates were incubated in a 5% CO_2 incubator at 37°C for 12 hours to allow cellular adhesion. Subsequently, 450 μl of medium with 10% FBS was added into each well for further incubation for 5 days, and the DMEM was changed once every 24 hours.

Primary hepatocytes were used as a mode motile cell line to evaluate the bio-NG–cell interaction that can stimulate and regulate the motility of motor cells. Hepatocytes (200 μl) were seeded onto the samples at a density of 10^6 cells/ml in each sample with DMEM culture medium. Then, the plates were incubated in a 5% CO_2 incubator at 37°C for 12 hours to allow cellular adhesion. Subsequently, 300 μl of fresh medium was added into each well for further incubation for 15 days, and the DMEM was changed once every 24 hours.

hMSCs (Lonza) were expanded to passage 4 in growth media containing α-MEM with 16.7% FBS, 1% glutamine, and 1% penicillin-streptomycin. hMSCs (2×10^4 cells/cm^2) were cultured on the 2D NGs and TCP. hMSCs [20 μl (2.0×10^5 cells)] were seeded into bio-NGs and 3D fibers for 2 hours for cell attachment before further cell culturing. Constructs were then cultured in osteogenic media [α-MEM, 16.67% FBS, 1% glutamine, 10 mM β-glycerophosphate disodium, ascorbate (50 mg/ml), and 100 nM dexamethasone], which was changed three times per week, and evaluated at selected time points.

RGC5 cell proliferation and apoptosis

DNA assay was performed to evaluate proliferation of RGC5 cells in bio-NGs. The cultured RGC5 cells were first put in a 1.5-ml centrifuge tube. The specific operation of DNA extraction was carried out in accordance with the steps of the standard instructions. After successful DNA extraction, the extracted DNA was placed in a cool place at room temperature and dried for 15 min. After being dissolved in 100 μl of PBS buffer, the OD_{260} value was determined on NanoDrop (2000, Thermo Fisher Scientific Co. Ltd.). The flow cytometer (NovoCyte, Aisen Biological Co. Ltd.) was used to excite cell apoptosis test staining solution at an excitation wavelength of 488 nm to detect cell apoptosis.

RGC5 cell morphology and adhesion analysis

To observe the morphology and attachment of RGC5 cells on the fibers in bio-NGs, photographs of RGC5 cells after 5 days in culture were collected using a laser scanning confocal microscope (SP8, Leica). To better observe the interaction between cells and fibers, fibers and RGC5 were stained with the fluorescent agent rhodamine B and the live cytoskeleton fluorescent dye calcein-AM, respectively. When performing 3D confocal scanning, the adhesion state between the NGs and the cells can be observed by simultaneously exciting rhodamine B (red) and calcein-AM (green). The cells were observed and analyzed using an inverted biological microscope (LWD200-37T, Shanghai Cewei Optoelectronics Technology Co. Ltd.).

RGC5 cell development and its Ca^{2+} channel

Because cells grow inside bio-NGs and the density of fibers in bio-NGs is high, it is difficult to visually observe the development details of cells including the neurite length and intracellular calcium concentration distribution. Therefore, we used medical tweezers to extract a small amount of fibers from bio-NGs and placed them on a glass slide for observation. The RGC5 cells were observed and analyzed using an inverted biological microscope (LWD200-37T, Shanghai Cewei Optoelectronics Technology Co. Ltd.). ImageJ was used to analyze the neurite length of the cells. To test the effect of NG-cell interaction on the Ca^{2+} in RGC5 neurons, the cells were loaded with Fluo-4 AM dye (Dojindo Laboratories, Japan) after 5 days in culture. Fluorescent images were acquired on a laser scanning confocal microscope (SP8, Leica).

Hepatocyte viability

The activity of the cultured hepatocytes was analyzed using an MTT assay every 24 hours. Briefly, the cells were firstly incubated with MTT solution in an incubator at 37°C for 3 hours. Then, the culture medium was removed, followed by the addition of dimethyl sulfoxide solvent into each well. The absorbance of the solution was measured using a microplate reader (Multiskan MK3, Thermo Fisher Scientific Inc.) at a wavelength of 490 nm.

Hepatocyte morphology and adhesion analysis and its motility

To observe the adhesion of cells to fibers in bio-NGs, photographs of hepatocytes after 3 days in culture were collected by SEM (Supra 55, Carl Zeiss). Hepatocytes cultured on different samples were fixed with 2.5% glutaraldehyde for 2 hours. A graded ethanol series (10, 20, 30, 50, 70, and 90%) was used to dehydrate the cells in sequence. The dried samples were sputter-coated with Au and observed with SEM. To observe the cell interaction within the cell aggregation, the E-CAD of the cells was stained with calcein (green). The calcein dye was excited with a 495-nm laser and observed under a laser scanning confocal microscope (SP8, Leica). The cell motility was evaluated by counting hepatocyte aggregate size and number. After 3 days in culture, we randomly observed 10 areas on each sample using an inverted microscope (LWD200-37T, Shanghai Cewei Optoelectronics Technology Co. Ltd.) and manually recorded the number of hepatocyte aggregates (diameter, >25 μm) and the diameter of hepatocyte aggregates.

Assessment of hepatic function

Alb secretion was determined by using the Rat Albumin ELISA Quantitation Kit (Bethyl Laboratories Inc., Montgomery, USA). Urea synthesis

by hepatocytes incubated in fresh medium containing 2 mM NH_4Cl for 90 min was measured with the Urea Nitrogen kit (BioChain Institute Inc., Boerne, USA). CYP1A enzymatic activity and UGT were assessed by the conversion of 50 mM CEC and 100 mM 4-MU (Sigma-Aldrich, USA) to CHC and 4-methylumbelliferyl glucuronide (4-MUG) in 60-min incubations, respectively. CHC and 4-MUG were detected at an excitation wavelength of 325 nm as previously described using capillary electrophoresis (P/ACE MDQ, Beckman Instruments Inc., USA).

Assessment of liver repair in vivo

Rats (150 to 200 g) were anesthetized by the intake of isoflurane gas (0.8 to 1.5%) and maintained with 1.0% isoflurane. We removed a cylindrical liver tissue with a diameter of 10 mm and a height of 6 mm from the middle part of the third lobe liver, resulting in acute liver injury. After that, the bio-NGs were implanted into the defect site and sutured with surgical thread. Before the implementation, bio-NGs were fully dispersed in stroke-physiological saline solution and sterilized with UV for 1 hour. Last, the implantation site was rinsed twice with saline, and then, the muscle and skin were sutured. The external wounds are treated with iodophor, and all rats were raised in accordance with the relevant regulations for experimental animals and given regular food and water. All the implants (1, 2, and 4 weeks) were dehydrated, then embedded in paraffin, and sliced by using a microtome. H&E staining, fibrin(ogen) immunostaining, and Alb immunostaining were used to evaluate inflammation, blood flow, and liver function expression levels in regenerated tissues, respectively. Liver repair level was evaluated by E-CAD immunostaining and GS immunostaining. All sections were counterstained with 4′,6-diamidino-2-phenylindole dihydrochloride before being mounted.

Assessment of in vivo application potential

In vivo biocompatibility was assessed by histological assessment of Masson staining and immunofluorescent TNF-α staining, respectively. Rats (100 to 200 g) were anesthetized by the intake of isoflurane gas (0.8 to 1.5%) and maintained with 1.0% isoflurane. Before the implementation of bio-NGs, bio-NGs were fully dispersed in stroke-physiological saline solution and sterilized with UV for 1 hour. Then, bio-NGs were implanted in the gastrocnemius area and around the sciatic nerve. All the implants (1, 2, 4, and 8 weeks) were dehydrated, then embedded in paraffin, and sliced by using a microtome. The Masson stains were used to mark the collagenous fiber in muscle tissue, and the TNF-α was used to mark the inflammation in the sciatic nerve. The observed image was obtained via an immunofluorescence microscope (SP8, Leica). All rats received humane care and were handled in accordance with Institutional Animal Care and Use Committee approval protocol of the Animal Care Center at the Nanjing Jinling Hospital.

SUPPLEMENTARY MATERIALS

Supplementary material for this article is available at https://science.org/doi/10.1126/sciadv.abh2350

View/request a protocol for this paper from *Bio-protocol*.

REFERENCES AND NOTES

1. G. Thrivikraman, S. K. Boda, B. Basu, Unraveling the mechanistic effects of electric field stimulation towards directing stem cell fate and function: A tissue engineering perspective. *Biomaterials* **150**, 60–86 (2018).
2. J. L. Ruan, N. L. Tulloch, M. V. Razumova, M. Saiget, V. Muskheli, L. Pabon, H. Reinecke, M. Regnier, C. E. Murry, Mechanical stress conditioning and electrical stimulation promote contractility and force maturation of induced pluripotent stem cell-derived human cardiac tissue. *Circulation* **134**, 1557–1567 (2016).
3. Z. Q. Feng, T. Wang, B. Zhao, J. Li, L. Jin, Soft graphene nanofibers designed for the acceleration of nerve growth and development. *Adv. Mater.* **27**, 6462–6468 (2015).
4. Q. Zheng, Q. Tang, Z. L. Wang, Z. Li, Self-powered cardiovascular electronic devices and systems. *Nat. Rev. Cardiol.* **18**, 7–21 (2021).
5. P. M. Mendes, Cellular nanotechnology: Making biological interfaces smarter. *Chem. Soc. Rev.* **42**, 9207–9218 (2013).
6. E. Bressan, L. Ferroni, C. Gardin, L. Sbricoli, L. Gobbato, F. S. Ludovichetti, I. Tocco, A. Carraro, A. Piattelli, B. Zavan, Graphene based scaffolds effects on stem cells commitment. *J. Transl. Med.* **12**, 296 (2014).
7. G. Yao, D. Jiang, J. Li, L. Kang, S. Chen, Y. Long, Y. Wang, P. Huang, Y. Lin, W. Cai, X. Wang, Self-activated electrical stimulation for effective hair regeneration via a wearable omnidirectional pulse generator. *ACS Nano* **13**, 12345–12356 (2019).
8. G. Yao, L. Kang, J. Li, Y. Long, H. Wei, C. A. Ferreira, J. J. Jeffery, Y. Lin, W. Cai, X. Wang, Effective weight control via an implanted self-powered vagus nerve stimulation device. *Nat. Commun.* **9**, 5349 (2018).
9. Y. Long, H. Wei, J. Li, G. Yao, B. Yu, D. Ni, A. L. F. Gibson, X. Lan, Y. Jiang, W. Cai, X. Wang, Effective wound healing enabled by discrete alternative electric fields from wearable nanogenerators. *ACS Nano* **12**, 12533–12540 (2018).
10. T. Li, M. Qu, C. Carlos, L. Gu, F. Jin, T. Yuan, X. Wu, J. Xiao, T. Wang, W. Dong, X. Wang, Z.-Q. Feng, High-performance poly(vinylidene difluoride)/dopamine core/shell piezoelectric nanofiber and its application for biomedical sensors. *Adv. Mater.* **33**, e2006093 (2020).
11. T. Li, Z. Q. Feng, M. Qu, K. Yan, T. Yuan, B. Gao, T. Wang, W. Dong, J. Zheng, Core/shell piezoelectric nanofibers with spatial self-orientated β-phase nanocrystals for real-time micropressure monitoring of cardiovascular walls. *ACS Nano* **13**, 10062–10073 (2019).
12. R. McBeath, D. M. Pirone, C. M. Nelson, K. Bhadriraju, C. S. Chen, Cell shape, cytoskeletal tension, and RhoA regulate stem cell lineage commitment. *Dev. Cell* **6**, 483–495 (2004).
13. T. Mseka, J. R. Bamburg, L. P. Cramer, ADF/cofilin family proteins control formation of oriented actin-filament bundles in the cell body to trigger fibroblast polarization. *J. Cell Sci.* **120**, 4332–4344 (2007).
14. K. Birmingham, V. Gradinaru, P. Anikeeva, W. M. Grill, V. Pikov, B. McLaughlin, P. Pasricha, D. Weber, K. Ludwig, K. Famm, Bioelectronic medicines: A research roadmap. *Nat. Rev. Drug Discov.* **13**, 399–400 (2014).
15. W. Li, J. Sigley, M. Pieters, C. C. Helms, C. Nagaswami, J. W. Weisel, M. Guthold, Fibrin fiber stiffness is strongly affected by fiber diameter, but not by fibrinogen glycation. *Biophys. J.* **110**, 1400–1410 (2016).
16. P. Singh, C. Carraher, J. E. Schwarzbauer, Assembly of fibronectin extracellular matrix. *Annu. Rev. Cell Dev. Biol.* **26**, 397–419 (2010).
17. R. M. Street, M. Minagawa, A. Vengrenyuk, C. L. Schauer, Piezoelectric electrospun polyacrylonitrile with various tacticities. *J. Appl. Polym. Sci.* **136**, 47530 (2019).
18. W. Wang, Y. Zheng, X. Jin, Y. Sun, B. Lu, H. Wang, J. Fang, H. Shao, T. Lin, Unexpectedly high piezoelectricity of electrospun polyacrylonitrile nanofiber membranes. *Nano Energy* **56**, 588–594 (2019).
19. D. Meng, M. Erol, A. R. Boccaccini, Processing technologies for 3D nanostructured tissue engineering scaffolds. *Adv. Eng. Mater.* **12**, B467–B487 (2010).
20. X. Zhang, X. Cui, D. Wang, S. Wang, Z. Liu, G. Zhao, Y. Zhang, Z. Li, Z. L. Wang, L. Li, Piezoelectric nanotopography induced neuron-like differentiation of stem cells. *Adv. Funct. Mater.* **29**, 1900372 (2019).
21. M. Minagawa, T. Taira, Y. Yabuta, K. Nozaki, F. Yoshii, An anomalous tacticity–crystallinity relationship: A WAXD study of stereoregular isotactic (83–25) poly(acrylonitrile) powder prepared by urea clathrate polymerization. *Macromolecules* **34**, 3679–3683 (2001).
22. J. T. Elliott, J. T. Woodward, A. Umarji, Y. Mei, A. Tona, The effect of surface chemistry on the formation of thin films of native fibrillar collagen. *Biomaterials* **28**, 576–585 (2007).
23. A. M. Greiner, B. Richter, M. Bastmeyer, Micro-engineered 3D scaffolds for cell culture studies. *Macromol. Biosci.* **12**, 1301–1314 (2012).
24. G. Murillo, A. Blanquer, C. Vargas-Estevez, L. Barrios, E. Ibáñez, C. Nogués, J. Esteve, Electromechanical nanogenerator-cell interaction modulates cell activity. *Adv. Mater.* **29**, 1605048 (2017).
25. B. Li, J. H. Wang, Application of sensing techniques to cellular force measurement. *Sensors* **10**, 9948–9962 (2010).
26. W. Wang, J. Li, H. Liu, S. Ge, Advancing versatile ferroelectric materials toward biomedical applications. *Adv. Sci.* **8**, 2003074 (2020).
27. A. Wang, Z. Liu, M. Hu, C. Wang, X. Zhang, B. Shi, Y. Fan, Y. Cui, Z. Li, K. Ren, Piezoelectric nanofibrous scaffolds as in vivo energy harvesters for modifying fibroblast alignment and proliferation in wound healing. *Nano Energy* **43**, 63–71 (2018).

28. L. Khatib, D. E. Golan, M. Cho, Physiologic electrical stimulation provokes intracellular calcium increase mediated by phospholipase C activation in human osteoblasts. *FASEB J.* **18**, 1903–1905 (2004).
29. M. Zayzafoon, Calcium/calmodulin signaling controls osteoblast growth and differentiation. *J. Cell. Biochem.* **97**, 56–70 (2006).
30. N. Ozkucur, T. K. Monsees, S. Perike, H. Q. Do, R. H. Funk, Local calcium elevation and cell elongation initiate guided motility in electrically stimulated osteoblast-like cells. *PLOS ONE* **4**, e6131 (2009).
31. L. Du, T. Li, F. Jin, Y. Wang, R. Li, J. Zheng, T. Wang, Z.-Q. Feng, Design of high conductive and piezoelectric poly (3,4-ethylenedioxythiophene)/chitosan nanofibers for enhancing cellular electrical stimulation. *J. Colloid Interface Sci.* **559**, 65–75 (2020).
32. J. Tian, R. Shi, Z. Liu, H. Ouyang, M. Yu, C. Zhao, Y. Zou, D. Jiang, J. Zhang, Z. Li, Self-powered implantable electrical stimulator for osteoblasts' proliferation and differentiation. *Nano Energy* **59**, 705–714 (2019).
33. M. R. Cho, H. S. Thatte, R. C. Lee, D. E. Golan, Integrin-dependent human macrophage migration induced by oscillatory electrical stimulation. *Ann. Biomed. Eng.* **28**, 234–243 (2000).
34. R. Shi, J. Zhang, J. Tian, C. Zhao, Z. Li, Y. Zhang, Y. Li, C. Wu, W. Tian, Z. Li, An effective self-powered strategy to endow titanium implant surface with associated activity of anti-biofilm and osteogenesis. *Nano Energy* **77**, 105201 (2020).
35. Z. Q. Feng, X. H. Chu, N. P. Huang, M. K. Leach, G. Wang, Y. C. Wang, Y. T. Ding, Z. Z. Gu, Rat hepatocyte aggregate formation on discrete aligned nanofibers of type-I collagen-coated poly(L-lactic acid). *Biomaterials* **31**, 3604–3612 (2010).
36. Z. Q. Feng, X. Chu, N. P. Huang, T. Wang, Y. Wang, X. Shi, Y. Ding, Z. Z. Gu, The effect of nanofibrous galactosylated chitosan scaffolds on the formation of rat primary hepatocyte aggregates and the maintenance of liver function. *Biomaterials* **30**, 2753–2763 (2009).
37. L. Leppik, K. M. C. Oliveira, M. B. Bhavsar, J. H. Barker, Electrical stimulation in bone tissue engineering treatments. *Eur. J. Trauma Emerg. Surg.* **46**, 231–244 (2020).
38. Q. Xu, X. Gao, S. Zhao, Y.-N. Liu, D. Zhang, K. Zhou, H. Khanbareh, W. Chen, Y. Zhang, C. Bowen, Construction of bio-piezoelectric platforms: From structures and synthesis to applications. *Adv. Mater.* **33**, e2008452 (2021).
39. E. R. Andersson, In the zone for liver proliferation. *Science* **371**, 887–888 (2021).
40. L. He, W. Pu, X. Liu, Z. Zhang, M. Han, Y. Li, X. Huang, X. Han, Y. Li, K. Liu, M. Shi, L. Lai, R. Sun, Q. D. Wang, Y. Ji, J. S. Tchorz, B. Zhou, Proliferation tracing reveals regional hepatocyte generation in liver homeostasis and repair. *Science* **371**, eabc4346 (2021).
41. G. Zajicek, R. Oren, M. Weinreb Jr., The streaming liver. *Liver* **5**, 293–300 (1985).
42. H. Sekine, T. Shimizu, I. Dobashi, K. Matsuura, N. Hagiwara, M. Takahashi, E. Kobayashi, M. Yamato, T. Okano, Cardiac cell sheet transplantation improves damaged heart function via superior cell survival in comparison with dissociated cell injection. *Tissue Eng. Part A* **17**, 2973–2980 (2011).
43. Y. Morikawa, T. Heallen, J. Leach, Y. Xiao, J. F. Martin, Dystrophin-glycoprotein complex sequesters Yap to inhibit cardiomyocyte proliferation. *Nature* **547**, 227–231 (2017).
44. H. Hashimoto, E. N. Olson, R. Bassel-Duby, Therapeutic approaches for cardiac regeneration and repair. *Nat. Rev. Cardiol.* **15**, 585–600 (2018).
45. H. C. Chen, C. M. Liang, C. H. Wang, M. Y. Huang, Y. Y. Lin, C. P. Shih, C. Y. Kuo, Y. C. Lin, H. K. Chen, Transplantation of human limbus-derived mesenchymal stromal cells via occipital approach improves hearing in animal auditory neuropathy. *Int. J. Pediatr. Otorhinolaryngol.* **117**, 67–72 (2019).
46. D. O. Adewole, L. A. Struzyna, J. C. Burrell, J. P. Harris, A. D. Nemes, D. Petrov, R. H. Kraft, H. I. Chen, M. D. Serruya, J. A. Wolf, D. K. Cullen, Development of optically controlled "living electrodes" with long-projecting axon tracts for a synaptic brain-machine interface. *Sci. Adv.* **7**, eaay5347 (2021).
47. M. Ashrafi, T. Alonso-Rasgado, M. Baguneid, A. Bayat, The efficacy of electrical stimulation in experimentally induced cutaneous wounds in animals. *Vet. Dermatol.* **27**, 235-e57 (2016).
48. B. Reid, B. Song, C. D. McCaig, M. Zhao, Wound healing in rat cornea: The role of electric currents. *FASEB J.* **19**, 379–386 (2005).
49. A. E. Moran, M. H. Forouzanfar, G. A. Roth, G. A. Mensah, M. Ezzati, C. J. L. Murray, M. Naghavi, Temporal trends in ischemic heart disease mortality in 21 world regions, 1980 to 2010: The Global Burden of Disease 2010 study. *Circulation* **129**, 1483–1492 (2014).
50. M. A. Laflamme, C. E. Murry, Heart regeneration. *Nature* **473**, 326–335 (2011).
51. I. Batalov, A. W. Feinberg, Differentiation of cardiomyocytes from human pluripotent stem cells using monolayer culture. *Biomark. Insights* **10**, 71–76 (2015).
52. D. Hernandez, R. Millard, P. Sivakumaran, R. C. B. Wong, D. E. Crombie, A. W. Hewitt, H. Liang, S. S. C. Hung, A. Pébay, R. K. Shepherd, G. J. Dusting, S. Y. Lim, Electrical stimulation promotes cardiac differentiation of human induced pluripotent stem cells. *Stem Cells Int.* **2016**, 1718041 (2016).

Acknowledgments

Funding: The authors acknowledge financial support from the National Natural Science Foundation of China (51773093 and 11204033), Postgraduate Research and Practice Innovation Program of Jiangsu Province (SJCX17_0118), and the Fundamental Research Funds for the Central Universities (no. 30920041105). T.L. acknowledges financial support from the China Scholarship Council (CSC: 201906840093). **Author contributions:** T.L., C.S., F.J., and F.Y. contributed equally to this work. Z.-Q.F., T.L., and C.S. designed the research and wrote the manuscript. T.L., C.S., and F.J. performed and analyzed most experiments. F.Y. performed theoretical simulations. T.L., Z.-Q.F., F.J., L.G., T.W., and W.D. performed data analysis. All authors discussed the results and contributed to paper writing. **Competing interests:** The authors declare that they have no competing interests. **Data and materials availability:** All data needed to evaluate the conclusions in the paper are present in the paper and/or the Supplementary Materials.

Submitted 25 February 2021
Accepted 30 July 2021
Published 24 September 2021
10.1126/sciadv.abh2350

Citation: T. Li, C. Shi, F. Jin, F. Yang, L. Gu, T. Wang, W. Dong, Z.-Q. Feng, Cell activity modulation and its specific function maintenance by bioinspired electromechanical nanogenerator. *Sci. Adv.* **7**, eabh2350 (2021).